Research Article Vol. 4, No. 9 / September 2017 / Optica 1038

Self-optimization of plasmonic nanoantennas in strong femtosecond fields

Liping Shi,[1,2,*] Bianca Iwan,[1,3] Rana Nicolas,[3] Quentin Ripault,[3] Jose R. C. Andrade,[1] Seunghwoi Han,[4] Hyunwoong Kim,[4] Willem Boutu,[3] Dominik Franz,[3] Torsten Heidenblut,[5] Carsten Reinhardt,[6] Bert Bastiaens,[7] Tamas Nagy,[1,8] Ihar Babushkin,[1,9] Uwe Morgner,[1,2] Seung-Woo Kim,[4] Günter Steinmeyer,[9] Hamed Merdji,[3] and Milutin Kovacev[1,2,10]

[1]Institut für Quantenoptik, Leibniz Universität Hannover, Welfengarten 1, 30167 Hannover, Germany
[2]QUEST, Centre for Quantum Engineering and Space-Time Research, 30167 Hannover, Germany
[3]LIDYL, CEA, CNRS, Université Paris-Saclay, CEA Saclay, 91191 Gif-sur-Yvette, France
[4]Department of Mechanical Engineering, Korea Advanced Institute of Science and Technology (KAIST), Science Town, Daejeon 305-701, South Korea
[5]Institut für Werkstoffkunde, Leibniz Universität Hannover, An der Universität 2, 30823 Garbsen, Hannover, Germany
[6]Laser Zentrum Hannover e.V., Hollerithallee 8, D-30419 Hannover, Germany
[7]Laser Physics and Nonlinear Optics, Mesa+ Institute for Nanotechnology, University of Twente, Enschede, The Netherlands
[8]Laser-Laboratorium Göttingen e.V., Hans-Adolf-Krebs-Weg 1, D-37077 Göttingen, Germany
[9]Max-Born-Institut, Max-Born-Str. 2a, D-12489 Berlin, Germany
[10]e-mail: kovacev@iqo.uni-hannover.de
*Corresponding author: shi@iqo.uni-hannover.de

Received 14 March 2017; revised 3 August 2017; accepted 3 August 2017 (Doc. ID 290637); published 29 August 2017

Plasmonic dimer nanoantennas can significantly boost the electric field strength in the gap region, allowing for a modification of the feed gap geometry by femtosecond laser illumination. Using resonant bowtie antennas to enhance the electric field of a low-fluence femtosecond oscillator, here we experimentally demonstrate highly localized reshaping of the antennas, resulting in a self-optimization of the antenna shape. From high-resolution scanning electron micrographs and two-dimensional energy dispersive x-ray maps, we analyze the near-field enhanced subwavelength ablation at the nanotips and the resulting deposition of ablated materials in the feed gap. The dominant ablation mechanism is attributed to the nonthermal transient unbonding of atoms and electrostatic acceleration of ions. This process is driven by surface plasmon enhanced electron emission, with subsequent acceleration in the vacuum. This ablation is impeded in the presence of an ambient gas. A maximum of sixfold enhancement of the third-harmonic yield is observed during the reshaping process.

OCIS codes: (310.6628) Subwavelength structures, nanostructures; (240.4350) Nonlinear optics at surfaces; (190.2620) Harmonic generation and mixing; (240.6680) Surface plasmons.

https://doi.org/10.1364/OPTICA.4.001038

1. INTRODUCTION

Field enhancement by plasmonic nanoantennas promises access to strong-field nonlinear optics with high-repetition-rate nanojoule oscillator sources, including field-driven photoemission of electrons as well as generation of nonperturbative high harmonic generation (HHG) and incoherent deep-ultraviolet radiation [1–6]. The plasmon-assisted HHG from gas atoms is challenging [7], because first, the small volume of near-field enhancement limits the build-up of a coherent process, and second, the gold nanostructures do not withstand a strong laser field. Nevertheless, it has recently been reported that HHG can be emitted from bulk crystals with lower peak intensity with respect to gaseous media [8]. Meanwhile, the atom density of solids is typically 3 orders of magnitude greater than that of gases. Hence plasmonic-nanoantenna-assisted HHG is now attracting interest again, but from a crystalline solid state substrate instead of injected gases [9,10]. The HHG process typically requires a peak intensity above 10^{13} W/cm^2. At this intensity level, strong-field effects, such as surface nonthermal melting [11], nanoparticle reshaping [12], and ablation [13], accompanied by electron excitation and emission start to play an important role. These processes may change the morphology of the nanoantennas and thus influence the harmonic conversion efficiency. Therefore, in order to optimize the surface plasmon enhanced harmonic generation, it is crucial to investigate the modification of plasmonic metamaterials under the illumination of a femtosecond laser.

In this paper, we experimentally demonstrate a self-organized modification of gold bowtie nanoantennas during harmonic generation. Localized near-field enhanced ablation at the nanotips as

well as a rearrangement of material in the antenna hotspots is observed. It is shown that the modification of plasmonic nanoantennas through the irradiation of a femtosecond laser enables an additional boost of the harmonic conversion efficiency. Although the gaseous medium cannot support harmonic generation for our conditions, we found that it can be used to inhibit the ablation process.

2. EXPERIMENTS AND METHODS

Properly adjusting the bowtie geometry, skin layer currents in the side faces resonantly interact with the oscillating 820 nm driver field [Fig. 1(a)]. For the operating conditions of our mode-locked Ti:sapphire oscillator, a field enhancement factor of up to 20 is expected at the apex, enhancing the maximum field strength from incident 1.4 V/nm to 28 V/nm (0.25–100 TW/cm^2). The bowties are manufactured by focused ion beam milling on a sapphire substrate. Between the gold film and sapphire substrate, there is a 3-nm chromium layer to promote adhesion. The length and apex angle of a single gold triangle nanostructure are 175 nm and 30°, respectively. The dimers have a thickness of 135 nm and a gap size of 10 nm. The laser pulses from a femtosecond oscillator with a repetition rate of 100 MHz, energy of 0.8 nJ, and duration of 8 fs are tightly focused by an off-axis parabolic mirror onto an array of gold bowtie dimers. A pair of fused silica wedges and double-chirped mirrors are utilized to compensate the dispersion introduced by the air, the 0.4-mm sapphire substrate, and the 2-mm calcium fluoride optical window of the vacuum chamber. The focal length of the parabolic mirror is 20 cm. The laser polarization is parallel to the dimeric orientation. These nanostructures were arranged in square arrays of 12 μm × 12 μm, with a spacing of 500 nm in the x direction and 200 nm in the y direction. The field in the antenna gap (optical hot spot) is significantly amplified, leading to a dramatic enhancement of the third harmonic generation (THG) from the hot spot of the substrate surface [14]. The focal spot of the incident laser on the bowties has a diameter of 7 μm. This results in the simultaneous emission of THG from approximately 250 of the individual antennas,

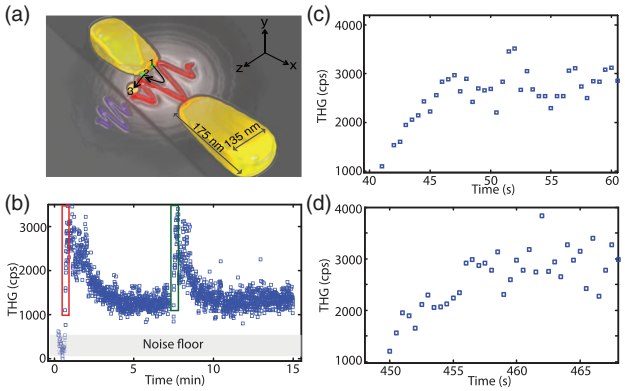

Fig. 1. (a) Illustration of a three-step process describing the erosion of the bowtie tip by a few-cycle laser (red transient). (1) An electron tunnels into the vacuum, (2) which is redirected back into the tip after one half-cycle and deposits its kinetic energy to locally heat the surface electron gas, which induces (3) unbonding and subsequent possible ejection of a gold atom. Surface THG (blue transient) is employed to probe the damage of bowtie tips. (b) Temporal evolution of THG emission from two fresh bowtie nanoantenna arrays in vacuum. The squares enclosed in red and green are enlarged in (c) and (d), respectively.

which is collected and measured by a toroidal grating combined with a photo multiplier. The sample is placed in a chamber with controllable pressure. We conducted a series of experiments, focusing our laser onto the antenna arrays both in vacuum and in nitrogen at ambient pressure.

3. EXPERIMENTAL RESULTS

First, placing the antennas in vacuum (10^{-3} mbar), we monitored the surface-plasmon-enhanced THG for sensing [15] the modification of the nanoantennas in real time [Fig. 1(b)]. Within 6 min, the signal rapidly decreased under continuous irradiation. After ~7 min, we translated the laser to irradiate a fresh antenna array. The THG recovered to its initial maximum, and then decreased again. Expanding the time axis [squares in Fig. 1(b)], we find that the THG signal increases within the first 15 s on a new position [Figs. 1(c) and 1(d)] before the degradation process sets in. This finding suggests that structural modification does not necessarily have a detrimental effect on the antenna function, but may also lead to a self-optimization and efficiency increase. Comparing the scanning electron microscopy (SEM) image of a pristine antenna pair [Fig. 2(b)], an evident change in the gap region is observed [Fig. 2(a)]. This observation implies that the observed ablation is closely related to the near-field enhancement.

For a deeper analysis of the chemical composition of the ablated material, a two-dimensional high-resolution energy-dispersive x-ray spectroscopy (EDX) measurement was performed in the gap of the irradiated antennas [Figs. 3(a)–3(g)], which is then compared to pristine antenna structures [Figs. 3(h)–3(n)]. This comparison reveals that the deposit includes evident gold [Fig. 3(a)], a high amount of silicon [Si, Fig. 3(b)], and some oxygen [O, Fig. 3(c)] as well as a small amount of carbon contamination [C, Fig. 3(d)]. The carbon component may arise due to cracking of spurious hydrocarbons. The Si might originate from the contamination on the substrate during the preparation and milling of the Au film. The emergence of gold atoms in the gap corroborates highly localized ablation at the antenna tips.

We repeated the THG measurements using fresh antennas in atmospheric nitrogen [Figs. 4(a) and 4(b)]. In strong contrast to vacuum conditions, the signal is observed to rapidly increase over time up to 10 min. We performed experiments at different pulse durations to further understand this remarkable self-optimization process. Figure 4(c) compares the temporal evolution of THG from two arrays illuminated with the same average power yet different pulse durations of 8 and 16 fs. We can see that the increase of pulse duration leads to a slower THG growth rate, indicating a gentler reshaping process. This finding further confirms that the structural modification of the antennas is caused by an optical effect, which depends on the peak intensity rather than on the average power-dependent plasmonic heating.

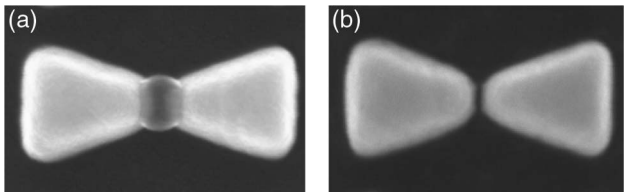

Fig. 2. SEM images of a (a) laser-ablated and (b) pristine gold bowtie antenna.

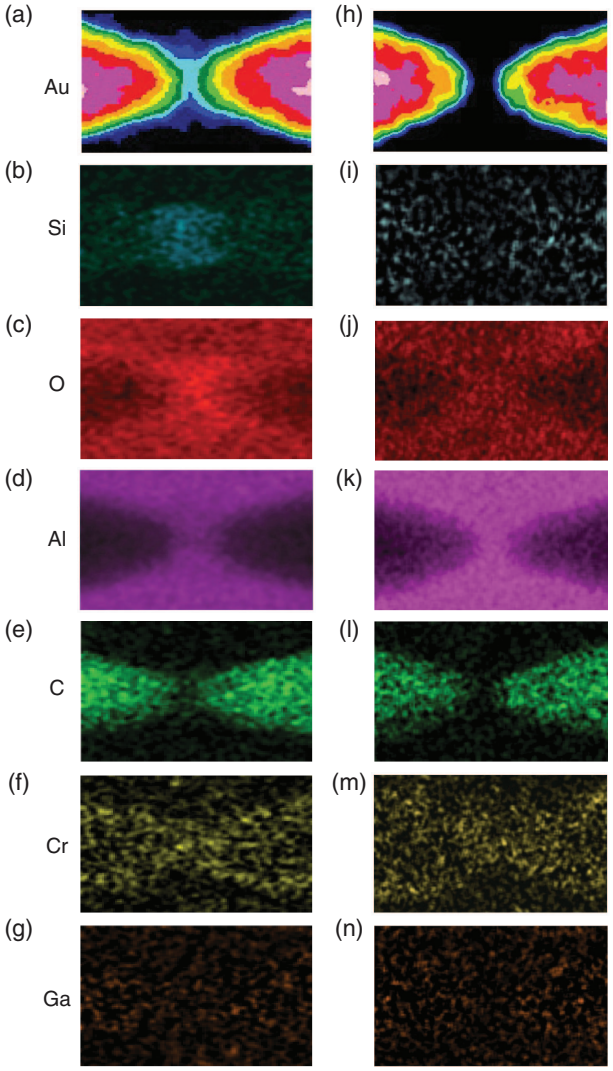

Fig. 3. Two-dimensional EDX maps of (a)–(g) laser-ablated antennas and (h)–(n) pristine antennas. The corresponding elements of the rows from top to bottom are Au, Si, O, Al, C, Cr, and Ga, respectively.

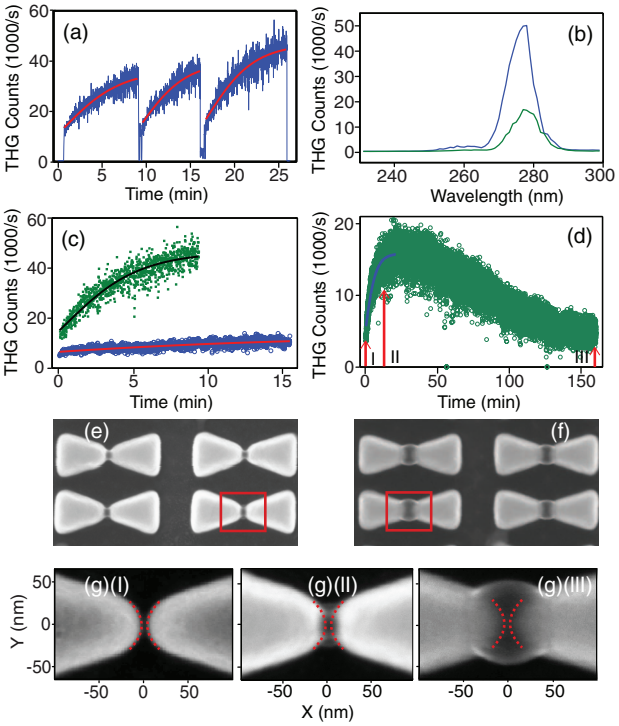

Fig. 4. (a) Temporal evolution of THG from three fresh arrays, which progressively increases over time. (b) THG spectra from the same array at the beginning (lower counts) and after 8 min of laser illumination in nitrogen (higher counts). (c) Evolution of THG with laser pulse duration of 8 fs (higher counts) and 16 fs (lower counts). (d) THG emission from a fresh array during long-term exposure. SEM image of antennas after (e) 8 min and (f) 165 min of laser irradiation in nitrogen, with the red squared areas enlarged in (g) (II) and (g) (III), respectively. Note that (g) (I–III) are enlarged SEM images corresponding to time frame I to III as indicated (red arrows) in (d), with the dashed curves sketching the initial profile of the tips.

In atmospheric nitrogen, the THG peaks after 25 min of illumination. Subsequently, it decreases slowly for 125 min until reaching a saturation that is still 50% higher than the initial flux [Fig. 4(d)]. The gradual reduction of THG implies that an ablation of the tips is occurring. Nevertheless, it is noticeable that the THG attenuation rate in nitrogen [Fig. 4(d)] is about 20 times slower than that of the vacuum [Fig. 1(b)], which verifies the inhibition of atom removal by nitrogen. Figure 4(e) and 4(f) show SEM images of the antennas after an illumination of 10 and 165 min, which are zoomed in Fig. 4(g)(II, III), respectively. It is evident that at an early stage reshaping only occurs at the apex, but eventually expands further outward after long-term exposure. This observation confirms again that the ablation is caused by a nonlinear optical effect and starts from the highest field region.

4. DISCUSSION

The mechanisms of femtosecond laser ablation have been well established in the past decade [16,17]. The incident laser penetrates into the skin layer and transfers some part of its energy to the electrons [Fig. 5(a)]. Energetic electrons may escape from the surface, subsequently pulling out charged ions via electrostatic interaction (gentle ablation), or the electrons may transfer their thermal energy to the surrounding lattice by diffusion, giving rise to a thermal phase explosion (strong ablation) [18–21]. Thus, depending on the laser fluence, one can identify two ablation regimes. For a gold target irradiated by a Ti:sapphire laser, the dominant process is found to be the electrostatic (gentle) ablation for laser fluences lower than 5 J/cm^2, and strong ablation is dominant at higher fluences [22]. In our experiments, considering the maximum enhanced laser fluence in the feed gap to be 0.8 J/cm^2 [Fig. 5(b)], we believe that the observed damage of bowtie tips can be solely ascribed to the gentle ablation mechanism.

Due to the ultrashort pulse duration of 8 fs in our experiments, the peak intensity at the bowtie tips exceeds 10^{14} W/cm^2, corresponding to an electric field strength of 28 V/nm. At this intensity level, nonlinear optical effects such as electron excitation, photoionization, and electron emission are significant during the pulse time. In order to evaluate their relative contribution, we compute the Keldysh parameter [23],

$$\gamma = \omega \frac{\sqrt{2m_e\phi}}{q_e E}, \quad (1)$$

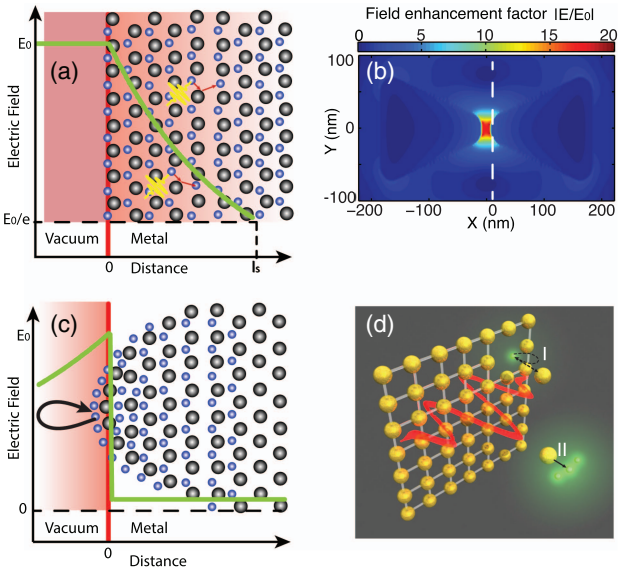

Fig. 5. (a) Schematic illustration of the electric field distribution (green curve) when a laser illuminates a bulk metal. Free electrons (blue spheres) in the skin layer are accelerated by the electric field of light wave (yellow curve) and experience collisional heating (red arrow). (b) Finite-difference time-domain (FDTD)-based numerical simulation of electric near-field distribution of a gold bowtie nanoantenna. The dashed white line denotes the interface between the vacuum and gold surface. (c) Schematic illustration of the field distribution (green curve) of the plasmonic nanoantenna. The electric field is significantly enhanced in the vacuum, peaks at the interface (red line), and dramatically decreases inside the metal. In addition to collisional heating, electron emission from the surface and subsequent collisionless vacuum heating (black arrow) should also be considered. The significant near-field enhancement caused by the plasmon resonance can assist a nanoscale subwavelength ablation at the surface layer. (d) Schematic illustration of two possible near-field enhanced ablation processes at the surface layer of the gold nanoantenna. I: Brunel electrons deposit energy into the surface, causing the nonthermal transient unbonding of atoms. II: electrostatic acceleration induced by charge separation.

where $\omega = 2.35 \times 10^{15}$ rad/s is the angular frequency of the driver field, ϕ is the work function of gold (4.83 eV), and E is the electric field strength. m_e and q_e are the electron mass and charge, respectively. For the field enhancement in the feed gap, we compute $\gamma = 0.6$, i.e., tunneling of hot electrons from the gold antennas into the vacuum becomes a possible process, which is nevertheless restricted to the feed gap. As we will detail below, the presence of electron emission initiates a sequence of processes that may eventually lead to tip-selective ablation of the gold bowtie antennas.

As predicted by the Fowler–Nordheim equation, the electron tunneling probability is [24]

$$t(E) = \exp\left(-\frac{8}{3}\frac{\sqrt{2q_e m_e}}{\hbar E}\phi^{\frac{3}{2}}\right). \quad (2)$$

Here $\hbar$ is the Planck constant. For the above-mentioned field strength of 28 V/nm, about 1% of the electrons are expected to tunnel out into the vacuum within the central negative field cycles. After initial tunneling, the electrons are accelerated away from the surface, as the laser polarization is perpendicular to the surface, and the field strength is significantly enhanced in the feed gap. A portion of electrons are eventually thrown back onto the surface at the end of the subsequent half-cycle [Fig. 5(c), black arrow], i.e., a process called Brunel heating [25], as it causes additional excitation of the surface [26]. In this process, the Brunel electrons can obtain a maximum kinetic energy $E_{\text{kin}} = 0.8q_e^2E^2/m_e\omega^2 \sim 23$ eV for our experimental conditions. Some part of this energy is deposited into the electron gas at the metal surface. As a result, the excitation of surface electrons by the laser field as well as the returned energetic electrons result in a sudden potential energy of the surface atoms, which can thus be instantaneously unbound [process I in Fig. 5(d)] [11,12,16,27]. The deposited electron energy is expected to diffuse into the bulk on a subpicosecond time scale. During this temporal window, a small amount of energy can be transferred into the gold atom, and the lattice is expected to remain near room temperature. According to the Maxwell–Boltzmann distribution, the initial averaged thermal velocity of gold atoms at 300 K is 110 m/s, which does not suffice to transverse the unit cell size of gold ($a = 408$ pm) and eject them from the surface during the subpicosecond time. Therefore, most of the transiently unbound surface atoms might be rearranged due to the change of surface tension, but they remain at the surface [11,28]. Nevertheless, there might exist very few atoms with initial thermal velocity normal to the surface exceeding several hundred meters per second that can escape from the surface during a subpicosecond time window. Such cold ablation [29,30] events are rather rare, occurring only after one out of a million initial tunneling events.

A second channel of gold ablation comes from the electrostatic interaction with the tunneling electrons that remain at a positive velocity in the vacuum after the femtosecond pulse [21,31,32]. Furthermore, the collision of returned electrons is expected to be elastic and to create secondary energetic electrons with about 40% probability [33] for the impact energy ranging from 10 to 20 eV. The escaped electrons cloud produces an electrostatic field [process II in Fig. 5(d)] between the electrons and the positively charged surface. This induced field can accelerate and even pull the ions out of the solid if the electron energy is greater than the binding energy $\varepsilon_b = 8.2$ eV of gold ions. The time for a gold ion to acquire the binding energy, i.e., the escape time is [31]

$$t_{\text{esc}} \approx \frac{2}{\omega_{pe}}\left(\frac{m_{Au}}{m_e}\right)^{\frac{1}{2}}\left(\frac{\varepsilon_{\text{esc}}}{\varepsilon_{\text{esc}} - \varepsilon_b}\right)^{\frac{1}{2}}. \quad (3)$$

Here $\omega_{pe} = 1.3 \times 10^{16}$ Hz is the electron plasma frequency of gold, and $m_{Au} = 3.3 \times 10^{-25}$ kg is the gold atom mass. Assuming a reasonable kinetic energy of an electron $\varepsilon_{\text{esc}} = 10$ eV for our experimental conditions, the escape time of a gold ion is estimated to be $t_{\text{esc}} = 220$ fs, which also indicates a cold ablation process.

In both of the above-mentioned ablation processes, only a few gold atoms or ions in the Boltzmann tail can escape, which is in agreement with our observed rather low ablation rate. For example, from the high-resolution SEM images [Figs. 2(a) and 4(g) (II, III)], we conclude that only a few nanometers of gold were removed from the tips after minutes of irradiation. In other words, one needs more than 10^{10} pulses to remove several surface layers at the tips. This rate is several orders of magnitude lower than the ablation of bulk gold induced by an amplified laser at comparable peak intensities [31]. Furthermore, both ablation mechanisms take place on a time scale shorter than the electron–phonon coupling time. Therefore, the ablation process is of a nonequilibrium nature, which is also supported by our

findings, i.e., no collateral thermal damage of the gold antennas was observed.

As electron tunneling and subsequent Brunel heating is a highly nonlinear optical process, the strongest ablation will certainly appear in regions with the highest field enhancement, i.e., start to erode the center of the tip [Fig. 4(g)(II)]. The removal of atoms in the center may lead to a decrease of the radius of curvature in off-center regions, which leaves a surface with rather homogeneous curvature and widens the effective interaction zone. Such a structural self-optimization process might increase the THG yield at the onset of irradiation [Figs. 1(c) and 1(d)]. Furthermore, the deposition of silicon or silicon oxide in the feed gap may also act as an efficient nonlinear optical medium and contribute to the enhancement of THG. Indeed, plasmon-enhanced generation of deep-ultraviolet photons from silicon has been reported very recently [10]. With further laser illumination, the ablation also occurs off-center [Figs. 2(a) and 4(g)(III)]. As a result, the tips are modified, and the radius of curvature at the tips is finally increased. The field enhancement factor gradually decreases with the increase of the curvature radius. The ablation eventually ceases when the field enhancement factor is lower than the ablation threshold. This explains the observed exponential decrease of THG and final saturation after 5 min of irradiation [Fig. 1(b)]. Moreover, the higher ablation rate in the tip center with respect to the off-center region also explains the rapid increase of THG at the beginning of the irradiation time, whereas it shows a slow decrease afterwards.

At atmospheric pressure, the gold atoms will experience collisions with ambient gas molecules, causing a large fraction of the gold atoms to be redirected back to the antenna surfaces. This effect is widely similar to the reduced thermal evaporation rate under non-vacuum conditions, as it is commonly exploited to reduce evaporation effects, e.g., of tungsten filaments in incandescent lamps. Therefore, the ablation rate at ambient pressure is markedly lower than in vacuum. The observed increase of the THG yield persists for several minutes in nitrogen [Fig. 4(a)], while it lasts only 15 s in vacuum [Figs. 1(c) and 1(d)].

5. CONCLUSION AND OUTLOOK

In this work, we identified surface plasmon enhanced electron emission and subsequent electrostatic interaction as the primary mechanism leading to a slow ablation process of gold plasmonic nanoantennas. While the ablation process, in vacuum, leads to a rapid reshaping that first optimizes and subsequently degrades the antennas in vacuum, we observe a longer-term self-optimization of the antenna tips under ambient pressure. It also appears possible to further reduce damage by reducing the efficiency of electron emission and recollision, e.g., by coating the structures with a dielectric film filling or by using higher gas pressure. In particular, the latter measure could be initiated after self-optimization of the nanoantennas. A second interesting aspect of this work is the rather slow ablation process, which leads to a very narrow energy distribution of the ablated atoms. This process could be exploited for generating single atoms with very well-defined velocities for spectroscopic experiments. In summary, we believe that the cold ablation process and the self-optimization of the nanoantennas open new perspectives for a number of applications in nonlinear optics, atom optics, and spectroscopy.

Funding. Deutsche Forschungsgemeinschaft (DFG) (KO 3798/4-1); Centre for Quantum Engineering and Space-Time Research (QUEST), from Lower Saxony through "Quanten- und Nanometrologie" (QUANOMET, Project Nanophotonik); National Research Foundation of Korea (NRF) (NRF-2012R1A3A1050386); Agence Nationale de la Recherche (ANR) (IPEX); LABEX PALM (ANR-10-LABX-0039, Plasmon-X, HILAC); Vetenskapsrådet (VR) (637-2013-439).

Acknowledgment. Liping Shi is grateful to Jeremy Baumberg from University of Cambridge for stimulating discussions.

REFERENCES

1. M. Kauranen and A. V. Zayats, "Nonlinear plasmonics," Nat. Photonics **6**, 737–748 (2012).
2. J. A. Schuller, E. S. Barnard, W. Cai, Y. C. Jun, J. S. White, and M. L. Brongersma, "Plasmonics for extreme light concentration and manipulation," Nat. Mater. **9**, 193–204 (2010).
3. G. Herink, D. Solli, M. Gulde, and C. Ropers, "Field-driven photoemission from nanostructures quenches the quiver motion," Nature **483**, 190–193 (2012).
4. M. Krüger, M. Schenk, and P. Hommelhoff, "Attosecond control of electrons emitted from a nanoscale metal tip," Nature **475**, 78–81 (2011).
5. S. Kim, J. Jin, Y.-J. Kim, I.-Y. Park, Y. Kim, and S.-W. Kim, "High-harmonic generation by resonant plasmon field enhancement," Nature **453**, 757–760 (2008).
6. N. Pfullmann, C. Waltermann, M. Noack, S. Rausch, T. Nagy, C. Reinhardt, M. Kovačev, V. Knittel, R. Bratschitsch, D. Akemeier, A. Hutten, A. Leitenstorfer, and U. Morgner, "Bow-tie nano-antenna assisted generation of extreme ultraviolet radiation," New J. Phys. **15**, 093027 (2013).
7. M. Sivis, M. Duwe, B. Abel, and C. Ropers, "Extreme-ultraviolet light generation in plasmonic nanostructures," Nat. Phys. **9**, 304–309 (2013).
8. T. T. Luu, M. Garg, S. Y. Kruchinin, A. Moulet, M. T. Hassan, and E. Goulielmakis, "Extreme ultraviolet high-harmonic spectroscopy of solids," Nature **521**, 498–502 (2015).
9. S. Han, H. Kim, Y. W. Kim, Y.-J. Kim, S. Kim, I.-Y. Park, and S.-W. Kim, "High-harmonic generation by field enhanced femtosecond pulses in metal-sapphire nanostructure," Nat. Commun. **7**, 13105 (2016).
10. G. Vampa, B. Ghamsari, S. S. Mousavi, T. Hammond, A. Olivieri, E. Lisicka-Skrek, A. Y. Naumov, D. Villeneuve, A. Staudte, P. Berini, and P. Corkum, "Plasmon-enhanced high-harmonic generation from silicon," Nat. Phys. **13**, 659–662 (2017).
11. L. O. Herrmann, V. K. Valev, C. Tserkezis, J. S. Barnard, S. Kasera, O. A. Scherman, J. Aizpurua, and J. J. Baumberg, "Threading plasmonic nanoparticle strings with light," Nat. Commun. **5**, 4568 (2014).
12. A. Hu, Y. Zhou, and W. Duley, "Femtosecond laser-induced nanowelding: fundamentals and applications," Open Surf. Sci. J. **3**, 42–49 (2011).
13. A. Plech, V. Kotaidis, M. Lorenc, and J. Boneberg, "Femtosecond laser near-field ablation from gold nanoparticles," Nat. Phys. **2**, 44–47 (2006).
14. H. Aouani, M. Rahmani, M. Navarro-Ca, and S. A. Maier, "Third-harmonic-upconversion enhancement from a single semiconductor nanoparticle coupled to a plasmonic antenna," Nat. Nanotechnol. **9**, 290–294 (2014).
15. M. Mesch, B. Metzger, M. Hentschel, and H. Giessen, "Nonlinear plasmonic sensing," Nano Lett. **16**, 3155–3159 (2016).
16. B. Rethfeld, D. S. Ivanov, M. E. Garcia, and S. I. Anisimov, "Modelling ultrafast laser ablation," J. Phys. D **50**, 193001 (2017).
17. E. G. Gamaly, "The physics of ultra-short laser interaction with solids at non-relativistic intensities," Phys. Rep. **508**, 91–243 (2011).
18. S. Musazzi and U. Perini, *Laser-Induced Breakdown Spectroscopy: Theory and Applications* (Springer, 2014), Vol. **182**.
19. S. Amoruso, X. Wang, C. Altucci, C. De Lisio, M. Armenante, R. Bruzzese, and R. Velotta, "Thermal and nonthermal ion emission during high-fluence femtosecond laser ablation of metallic targets," Appl. Phys. Lett. **77**, 3728–3730 (2000).
20. K. Furusawa, K. Takahashi, H. Kumagai, K. Midorikawa, and M. Obara, "Ablation characteristics of Au, Ag, and Cu metals using a femtosecond Ti:sapphire laser," Appl. Phys. A **69**, S359–S366 (1999).

21. A. Rode, E. Gamaly, B. Luther-Davies, B. Taylor, J. Dawes, A. Chan, R. Lowe, and P. Hannaford, "Subpicosecond laser ablation of dental enamel," J. Appl. Phys. **92**, 2153–2158 (2002).
22. M. Shaheen, J. Gagnon, and B. Fryer, "Femtosecond laser ablation behavior of gold, crystalline silicon, and fused silica: a comparative study," Laser Phys. **24**, 106102 (2014).
23. L. Keldysh, "Ionization in the field of a strong electromagnetic wave," Sov. Phys. JETP **20**, 1307–1314 (1965).
24. R. H. Fowler and L. Nordheim, "Electron emission in intense electric fields," in *Proceedings of the Royal Society of London A: Mathematical, Physical and Engineering Sciences* (The Royal Society, 1928), Vol. **119**, pp. 173–181.
25. F. Brunel, "Not-so-resonant, resonant absorption," Phys. Rev. Lett. **59**, 52–55 (1987).
26. J. Weisshaupt, V. Juvé, M. Holtz, M. Woerner, and T. Elsaesser, "Theoretical analysis of hard x-ray generation by nonperturbative interaction of ultrashort light pulses with a metal," Struct. Dyn. **2**, 024102 (2015).
27. S. Sundaram and E. Mazur, "Inducing and probing non-thermal transitions in semiconductors using femtosecond laser pulses," Nat. Mater. **1**, 217–224 (2002).
28. J. Kern, R. Kullock, J. Prangsma, M. Emmerling, M. Kamp, and B. Hecht, "Electrically driven optical antennas," Nat. Photonics **9**, 582–586 (2015).
29. H. Mamin, S. Chiang, H. Birk, P. Guethner, and D. Rugar, "Gold deposition from a scanning tunneling microscope tip," J. Vac. Sci. Technol. B **9**, 1398–1402 (1991).
30. M. Hada, D. Zhang, K. Pichugin, J. Hirscht, M. A. Kochman, S. A. Hayes, S. Manz, R. Y. Gengler, D. A. Wann, T. Seki, G. Moriena, C. A. Morrison, J. Matsuo, G. Sciaini, and R. J. D. Miller, "Cold ablation driven by localized forces in alkali halides," Nat. Commun. **5**, 3863 (2014).
31. E. G. Gamaly, A. V. Rode, B. Luther-Davies, and V. T. Tikhonchuk, "Ablation of solids by femtosecond lasers: ablation mechanism and ablation thresholds for metals and dielectrics," Phys. Plasmas **9**, 949–957 (2002).
32. E. G. Gamaly, A. V. Rode, V. T. Tikhonchuk, and B. Luther-Davies, "Electrostatic mechanism of ablation by femtosecond lasers," Appl. Surf. Sci. **197**, 699–704 (2002).
33. R. L. Petry, "Secondary electron emission from tungsten, copper and gold," Phys. Rev. **28**, 362–366 (1926).